Article

Analysis of the Northern Hemisphere Atmospheric Circulation Response to Arctic Ice Reduction Based on Simulation Results

Gennady Platov [1]*, Vladimir Krupchatnikov [1], Viacheslav Gradov [1], Irina Borovko [1] and Evgeny Volodin [2]

[1] Institute of Computational Mathematics and Mathematical Geophysics, SB RAS; platov.g@gmail.com (G.P.); vkrupchatnikov@yandex.ru (V.K.); gradov.v.s@gmail.com (V.G.); irina.borovko@yandex.ru (I.B.)
[2] Marchuk Institute of Numerical Mathematics, RAS; volodinev@gmail.com
* Correspondence: platov.g@gmail.com

Abstract: The amplified Arctic warming is one of several factors influencing atmospheric dynamics. In this work, we consider a series of numerical experiments to identify the direct role of the Arctic sea ice reduction process in forming climatic trends in the northern hemisphere. Aimed at this, we used two more or less independent mechanisms of ice reduction. The first is traditionally associated with increasing the concentration of carbon dioxide in the atmosphere from the historic level of 360 ppm to 450 ppm and 600 ppm. This growth increases air temperature and decreases the ice volume. The second mechanism is associated with a reduction in the reflectivity of ice and snow. We assume that comparing the results of these two experiments allows us to judge the direct role of ice reduction. The most prominent consequences of ice reduction, as a result, were the weakening of temperature gradient at the tropopause level in mid-latitudes, the slower zonal wind at 50-60°N, intensification of wave activity in Europe, Western America, and Chukotka, and its weakening in the south of Siberia and Kazakhstan. We also consider how climate change may alter regimes such as blocking and stationary Rossby waves. The study used the INM-CM48 climate system model [1].

Keywords: sea ice; atmospheric circulation; Rossby waves; climate changes; Arctic; numerical modeling

1. Introduction

Since the mid-20th century, the Arctic has experienced two significant impacts of climate change: warming faster than average global warming and reducing winter and summer sea ice cover. However, the effect of melting sea ice in the Arctic on the global climate remains a matter of debate, particularly its impact on the Atlantic meridional overturning circulation (AMOC).

The reaction of large-scale atmospheric circulation in winter, which is formed as a result of the summer reduction in the area of floating ice, is characterized by an increase in the meridional component of flows in the atmosphere [2], reminiscent of the negative phase of the Arctic Oscillation (AO), which maintains cold winters in northern Eurasia [3]. Rossby waves with anomalously large amplitudes penetrate the stratosphere in February and weaken the stratospheric polar vortex [4–6], generating negative AO anomalies [7,8]. In addition, freshening of the subpolar Arctic due to sea ice melting reduces the intensity of AMOC [9] and associated heat transfer by ocean currents to the north [10], causing heat accumulation in tropical latitudes [11]. The resulting increase in ocean surface temperature in the tropics enhances deep atmospheric convection and associated latent heat release [12], leading to warming in the tropical upper troposphere.

Currently, there are still gaps in understanding the mechanisms linking Arctic warming, sea ice reduction, stratospheric-tropospheric interactions, and extreme weather events. The relationship between ice reduction and the corresponding changes in the structure of atmospheric circulation, established statistically or using numerical modeling, may not be

a relationship between cause and effect, but a relationship between two effects of some common cause, like atmospheric warming.

In the Arctic, the ice-albedo feedback mechanism plays a key role in the balance of heat and ice mass at the ocean surface [13,14]. During the melting season, the ice sheet changes its physical condition and optical properties. As the incident solar radiation increases and the air heats up, the ice sheet transforms from a highly diffuse snow-covered medium to a darker mix of bare ice and melt-ponds. Otherwise, the rate of summer thawing and the length of the thawing season are strongly influenced by albedo, which decreases as the melting season progresses. These changes decrease the surface albedo, resulting in greater absorption of solar energy at the surface, which increases surface warming and causes additional ice melting, known as sea ice-albedo feedback.

In this work, a series of numerical experiments aimed at identifying the direct role of the sea ice reduction process in forming climatic trends in the northern hemisphere is considered. We will use two more or less independent mechanisms for reducing ice in our numerical simulations. The first is traditionally associated with an increase in the concentration of carbon dioxide in the atmosphere above the historic level of 360 ppm. As a result of this increase, the average air temperature in the Arctic grows, and, by this, the volume of ice decreases. However, in this case, it is difficult to identify trends explicitly associated with ice reduction since the consequences arising from an increase in CO_2 and warming of the atmosphere can be more significant and obscure the role of ice reduction. The second experiment is associated with a decrease in the reflectivity of ice and snow – the amount of solar radiation absorbed by the ice increases, and its volume decreases. Under the conditions of this experiment, the change in the temperature of the atmosphere will be a consequence of the action of two competing processes: the atmosphere receives less reflected radiation but more long-wave radiation due to the higher surface temperature. When this article was almost ready, we found the recently published paper [15], which used a similar approach of ice-albedo decrease to analyze the consequences of Arctic ice reduction. We assume that comparing the results of these two experiments will make it possible to judge the direct role of ice reduction regardless of the reasons that caused this reduction. First of all, we will consider the sensitivity of atmospheric blocking and wave activity in mid-latitudes to Arctic ice variations.

Jet stream meanders are one of the main causes of weather variability at mid-latitudes. Large amplitudes of the meanders of the jet can cause extreme weather conditions. One way to quantify the jet stream meandering is to calculate the local wave activity (LWA) of finite amplitude as an amount of the displacement of the contour of the quasi-geostrophic potential vorticity [16]. LWA tends to be negatively correlated with zonal wind, and knowledge of regions of its high values is useful in identifying the localization of blocking events. Winds in the Earth's middle latitudes are directed mainly to the east, and their speed increases with height, forming a jet stream in the middle and upper troposphere. The jet stream carries cyclones and anticyclones, which in turn cause meandering of the jet stream. This wave structure also moves eastward, forming unsteady Rossby waves. Occasionally, however, the jet stream forms stable meanders in a specific area, disrupting the passage of non-stationary waves — a condition known as blocking.

Blockings are large-scale, quasi-stationary high-pressure anomalous systems (anticyclonic) that sometimes last for several weeks and block or deflect mid-latitude westerly winds [17–20]. Because of their duration and size, depending on the season and region, blocking events can trigger or contribute to various types of extreme events such as heatwaves, coldwaves, droughts, and episodes of heavy rainfall (eg. [21] and references therein). The contours of geopotential height 500 hPa and the wind speed determine the jet stream position, and its obvious deviation to the pole in the corresponding regions indicates blocking. In winter, in northern latitudes, blocking often occurs when a pre-existing quasi-stationary ridge becomes stronger and prevents the motion of non-stationary waves. While this suggests a role for stationary waves in blocking formation [22], the onset of blocking is still poorly understood and remains a complex issue in numerical weather prediction

[23,24]. The previously proposed mechanisms for the formation and maintenance of blockings include the action of unsteady vortices and the internal instability of low-frequency dynamics [25–29]. However, there is no definitive theory for the criterion for the occurrence of blocking. Furthermore, due to an incomplete understanding of the mechanisms, even the definition of blocking remains somewhat subjective [30,31].

2. Methods

2.1. Local Wave Activity

The key diagnostics for the interaction of vortices and mean flow is wave activity, a measure of the momentum carried by vortices [32]. Wave activity of finite amplitude was proposed as an objective measure for the spatial variation of a physical quantity, demonstrating monotonicity in the spatial distribution. Finite-amplitude wave activity (FAWA) [33–35] is a generalization of the linear wave activity of small amplitude waves.

FAWA (denoted as A^*) is defined as the area formed when the quasi-geostrophic potential vorticity (QGPV) contour q is displaced from its zonally symmetric state [34]:

$$A^*(\phi_e, z, t) = \frac{1}{2\pi a \cos\phi_e}\left[\iint\limits_{\substack{q\geq Q(\phi_e,z,t)\\ \frac{\pi}{2}\geq\phi}} q\,dS - \iint\limits_{\frac{\pi}{2}\geq\phi\geq\phi_e} q\,dS\right], \tag{1}$$

where ϕ_e is the equivalent latitude [36], defined so that the area in both integrals of the following equation would be the same, i.e. equal to Earth's area higher than ϕ_e:

$$\iint\limits_{\substack{q\geq Q(\phi_e,z,t)\\ \frac{\pi}{2}\geq\phi}} dS = \iint\limits_{\frac{\pi}{2}\geq\phi\geq\phi_e} dS = 2\pi a^2(1-\sin\phi_e), \tag{2}$$

where $z = -H\cdot\log(p/1000)$, and p is air pressure in hPa, H =7km is vertical scale, t is time, a =6378km is Earth's radius, q is QGPV defined as

$$q = f + \zeta + \frac{f}{\rho_0}\frac{\partial\left[\rho_0(\theta-\tilde{\theta})\frac{\partial\tilde{\theta}}{\partial z}\right]}{\partial z}, \tag{3}$$

f is Coriolis parameter, θ is potential temperature, $\tilde{\theta}$ is zonally averaged potential temperature, ρ_0 is reference air density, $Q(\phi_e, z, t)$ is Lagrangian mean of QGPV relative to the equivalent latitude ϕ_e at each z surface, and $dS = a^2\cos\phi\,d\lambda\,d\phi$, where λ is longitude.

Equation (1) is applied to vortices of arbitrary amplitude as the high limit of low amplitude waves, similar to the expression for linear waves [33].

Local wave activity (LWA) is a natural generalization of wave activity of finite amplitude regarding a specific range of longitudes. The precise definition of wave activity for potential vorticity and associated dynamic properties is detailed in [33,34]. Recently Huang and Nakamura [16,37] developed their variant of local wave activity and its associated balance for local wave phenomena such as wave breaking and blocking. Chen et al. [38] further extended the LWA concept to a less conserved value (viz. geopotential height of 500 hPa, designated as z_{500}) to facilitate its application. This approach is also adopted in our study. In particular, for z_{500}, which generally has a monotonic distribution in latitude, one can choose the value of its contour Z in the northern hemisphere so that the area S bounded by this Z contour and enclosing the North Pole will be

$$S(Z) = \iint\limits_{z_{500}\leq Z} a^2\cos\phi\,d\lambda\,d\phi. \tag{4}$$

We can determine the corresponding equivalent latitude ϕ_e surrounding the same area in the northern hemisphere. The following formula can establish a one-to-one relationship between ϕ_e and the Z value:

Preprints (www.preprints.org) | NOT PEER-REVIEWED | Posted: 11 August 2021 doi:10.20944/preprints202108.0261.v1

$$\phi_e = \arcsin\left[1 - \frac{S(Z)}{2\pi a^2}\right]. \tag{5}$$

We can introduce two components of LWA corresponding to ϕ_e and for each λ according to

$$\begin{aligned} A_S(\lambda, \phi_e) &= \frac{a}{\cos\phi_e} \int\limits_{\substack{z_{500} \le Z \\ \phi \le \phi_e}} (z_{500} - Z)\cos\phi \, d\phi, \\ A_N(\lambda, \phi_e) &= \frac{a}{\cos\phi_e} \int\limits_{\substack{z_{500} \ge Z \\ \phi \ge \phi_e}} (z_{500} - Z)\cos\phi \, d\phi. \end{aligned} \tag{6}$$

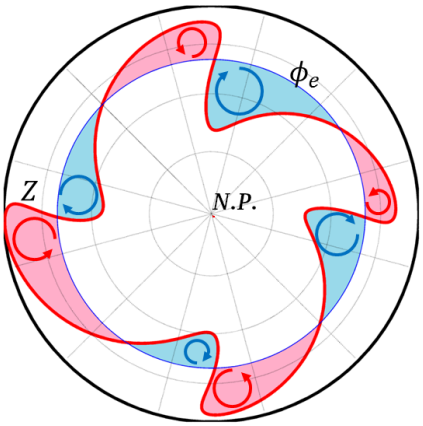

Figure 1. Configuration of areas around the North Pole, considered in Eq. 6. Z contour is represented by red curve, the corresponding equivalent latitude ϕ_e is blue circle. Red-shaded areas represent A_S integration area, and blue-shaded ones – A_N.

Both components A_N and $-A_S$, determined by (6), are positive definite (Figure 1). The former describes the activity of anticyclonic waves north of the equivalent latitude ϕ_e, and the latter describes the activity of cyclonic waves south of ϕ_e. Large and long-lasting A_N values are often associated with atmospheric blocking. The sum of A_N and $-A_S$ gives the total wave activity $A(\phi_e) = A_N - A_S$, which is a function of ϕ_e only. Thus, we return to the original meaning of wave activity as a quantity measuring the total waviness of the Z contour. A simple dimensional analysis shows that the overall wave activity can be estimated as $A \sim \frac{1}{2} l^2 \frac{dz_{500}}{dy}$. Thus, the wave activity can be considered as a result of the displacement of the z_{500} tracer by the meridional disturbance of scale l. The background gradient of this tracer is $\frac{dz_{500}}{dy}$. For a typical value of the gradient $\frac{dz_{500}}{d\phi_e}$ equal to 8 meters per degree of latitude and a meridional displacement of $\delta\phi \sim 15°$, the wave activity will be $A \sim 10^8$ m^2 [39].

2.2. Blocking event index

The interaction of the mean flow and vortices, which leads to the anomalous state of the mid-latitude jet, is associated with propagating and breaking waves in the upper troposphere and stratosphere. Extreme weather events in extratropical latitudes are usually associated with blocking anticyclones. We used the blocking diagnostics proposed by Tibaldi and Molteni (TM) in [40] and further developed in [41], which was used in [42] to obtain the main blocking areas for NCEP/NCAR reanalysis data. It is based on the gradients of the geopotential height. For each point with coordinates λ and ϕ, two indices could be determined as follows

$$\begin{aligned} \mathrm{GHGS}(\lambda,\phi) &= \frac{z_{500}(\lambda,\phi) - z_{500}(\lambda,\phi_S)}{\phi - \phi_S}, \\ \mathrm{GHGN}(\lambda,\phi) &= \frac{z_{500}(\lambda,\phi_N) - z_{500}(\lambda,\phi)}{\phi_N - \phi}, \end{aligned} \tag{7}$$

where $\phi_S = \phi - 15^\circ$, $\phi_N = \phi + 15^\circ$ and ϕ is central latitude of blocking and ranges from 15°N to 75°N. We consider a situation as instant blocking when

$$\begin{aligned} \mathrm{GHGS}(\lambda,\phi) &> 0, \\ \mathrm{GHGN}(\lambda,\phi) &< G_n, \end{aligned} \tag{8}$$

where G_n is taken to be equal to -5 m·(degree of latitude)$^{-1}$, although originally in [42] it was -10 m·(degree of latitude)$^{-1}$. In [43] a modified version of the TM index is used to diagnose and compare blockings in 15 models within the AMIP project, where it is required that $G_n = -5$ m·(degree of latitude)$^{-1}$. The reasons for this were related to the improved definition of the Pacific blocking. In this work, two main sectors of the Northern Hemisphere are distinguished, which from the point of view of observations are most susceptible to blocking, that is, the Euro-Atlantic and the Pacific, with the following longitudinal intervals: 26°W – 41°E and 115°E – 215°W correspondingly. The criterion $G_n = -10$ m·(degree of latitude)$^{-1}$ or less is stricter than TM and is desirable if we focus on stronger blockings.

3. Model and Experiments

The study used the INM-CM48 climate system model [1], developed at the INM RAS and considering many factors of climate change. The model can reproduce the dynamics of the atmosphere, sea ice, ocean, vegetation, and soils, taking into account greenhouse gases. Furthermore, unlike the previous version INM-CM4 [44], which was also used for experiments to reproduce climate change, an aerosol block was added to the model. As a result, the concentrations and radiation properties of 10 types of aerosols are interactively calculated. In contrast, the INM-CM4 model has prescribed distributions of aerosols and their properties. INM-CM48 includes a radiation block [45]. The model resolution used in our study in the atmospheric and aerosol modules is $2^\circ \times 1.5^\circ$ in longitude and latitude and 21 vertical levels, and in the ocean — $1^\circ \times 0.5^\circ$ and 40 levels.

Snow or ice albedo A is prescribed as $A = A_m$ in the case of melting ice or snow, $A = A_f$ in the case of surface temperature $T_s < T_f$, where T_f =263.15°K (or -10°C), and

$$A = A_f - \left(A_f - A_m\right)\frac{T_s - T_f}{T_m - T_f}$$

in the case $T_f < T_s < T_m$ (T_m is temperature of melting). Originally, $A_f = 0.8$ and $A_m = 0.6$ both for sea ice and snow, but these parameters are changed in sensitivity runs.

In our study, we carried out several numerical experiments using this model. The first B_0 is a baseline experiment which covers 100 years. In its run, following the data adopted for the historical experiment of CMIP6, we specified corresponding concentrations of greenhouse gases, emissions of anthropogenic aerosols, concentrations of volcanic aerosols, solar constant, and distribution of solar radiation over the spectrum.

The other four experiments cover the same period, but the experimental conditions have changed in the last 40 years. In one experiment A_1, we artificially lowered the albedo parameters of dry and wet ice (snow). Thus, the original values used in the model, 0.8 and 0.6, were reduced by 0.03 downto $A_f = 0.77$ and $A_m = 0.57$. In another experiment A_2 we reduce them even more down to 0.7 and 0.5. Experiments with the ice-albedo reduction in the CNRM-CM6-1 climate model were also analyzed in [15], but the albedo decreased down to the ocean albedo level, i.e., 0.07, and authors considered a short-term response to this reduction. In the following two experiments, we increased the concentration of carbon

dioxide in the atmosphere from the level of the B_0 experiment, which is 360 ppm, up to 450 ppm in one (C_1) and 600 ppm in the other (C_2).

Thus, in this study, we identify climate change caused by reducing summer sea ice to levels characteristic of global warming scenarios. We initiate this reduction of sea ice by artificially reducing its albedo, which changes the amount of shortwave radiation absorbed by the surface. We compare the results obtained with the response of the climate system to an increase in CO_2 emissions.

The loss of sea ice in the Arctic can affect the mid-latitude climate by altering large-scale circulation. Understanding to what extent we can consider climate change as changes caused by greenhouse gases or modulated by ice loss depends on how additive the responses to individual forcings are. Reducing sea ice albedo in a climate model can show to what extent the effects of increasing atmospheric carbon dioxide concentration and the loss of Arctic sea ice are additive and in which directions they can change the average climate state.

4. Results

The result of numerical experiments can be divided into three most essential parts. The first part intentionally demonstrates how the Arctic ice volume and its area changed depending on the experimental conditions. The second part demonstrates the changes in the zonal distribution of potential temperature and zonal velocity values with height. The third is associated with a change in the frequency of blocking situations in the atmospheric circulation and its connection with a change in the amount of ice.

4.1. Reduction of the ice volume and its area

Under experimental conditions, with a decrease in albedo A_1 and A_2, the amount of solar radiation absorbed by the surface increases, leading to a rise in the surface air temperature. Compared to the "base" experiment B_0, the surface air temperature in A_1 rose by 0.7°C in the Arctic and 0.17°C over the entire Earth. In A_2, the corresponding values are 1.7°C in the Arctic and 0.3°C globally. At the same time, the ice area decreased by 7% and its volume by 21% in the A_1 experiment, while in A_2 ice lost 3/4 of mass and 34% of its extent. In experiments with an increase in CO_2 concentration, ice melting occurs due to direct warming of the atmosphere because of the greenhouse effect. In the surface layer, the air temperature rise was approximately 0.97°C in C_1, which is close to A_1 and about two times lower than in the A_2 experiment. However, on average, its global growth was 0.45°C, which is substantially higher than in albedo experiments. The ice area in the C_1 experiment decreased by only 2.3%, and its volume reduced by 17% compared to the B_0 experiment. A more significant reduction in Arctic ice took place in the C_2 experiment with an increase in CO_2 concentration up to 600 ppm, where its area decreased by 10% and its volume by 23%. Thus the ice reduction is similar to the A_1 experiment. At the same time, the increase in averaged surface temperature is 1.0°C, and in the Arctic – 1.8°C. Therefore, the rise in the polar area is comparable to the A_2 experiment with albedo.

Table 1. Ice volume (1) and ice extent (2) seasonal minimum in percentage relative to B_0 experiment. Mean surface air temperature (SAT) increment: global (3) and in Arctic (4).

Experiment	(1), %	(2), %	(3), °C	(4), °C
A_1	79	93	0.17	0.70
A_2	25	66	0.30	1.7
C_1	83	98	0.45	0.97
C_2	77	90	1.0	1.8

4.2. Anomalies of zonal temperature distribution and zonal wind

The zonal distribution of atmospheric characteristics is most important in understanding its circulation. Figure 2 shows the zonal distribution of the potential temperature

anomaly with altitude according to the results of these last four experiments. The distributions have some similar features. The potential temperature has a noticeable increase of about 1°C in the lower troposphere above 60°N except for the A_1 experiment. Also, some increase occurs in the region of 30°N, which reaches the tropopause in altitude. In the stratosphere, the temperature has a reverse tendency of decrease by about 0.2°C in the 30-60°N band. The lower boundary of this anomaly deepens down to the level of the upper troposphere at 45-55°N.

The most noticeable difference is associated with changes in the polar part of the stratosphere. With a decrease in albedo, a positive anomaly of about 0.5-1.0°C arose there. This difference allows us to assume that the current decrease in ice in the Arctic contributes to an anomaly in this area.

On the contrary, in the upper troposphere over the equatorial part in C_1 and C_2 experiments, near-surface tropical warming is associated with strong tropical warming in the upper troposphere. The result is similar to [46] and can be explained by the change of moist adiabatic lapse rate. Thus, the positive anomaly is precisely a consequence of the greenhouse effect.

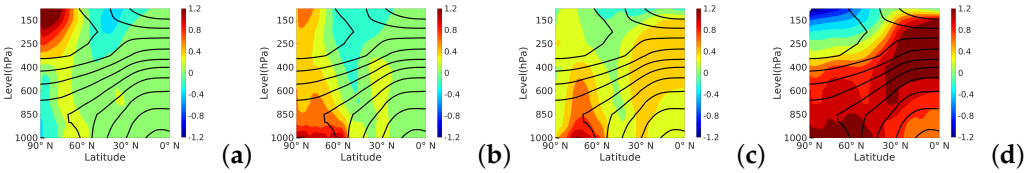

Figure 2. Anomalies of the zonal distribution of potential temperature resulted from averaging the winter (December-January-February) months over the last 30-year period. The isolines show the zonal distribution in the B_0 experiment. Color shading highlights the deviations in the A_1 experiment with an albedo reduced by 0.03 (**a**) and 0.1 in the A_2 experiment (**b**), in the C_1 experiment with an increase in CO_2 concentration to 450 ppm (**c**) and in the C_2 experiment with 600 ppm (**d**).

Figure 3 demonstrates the anomalies of the zonal velocity component. With a decrease in the ice-albedo, the zonal wind speed decreases near 50-60°N and increases in the subtropics. This structure corresponds to negative values of the Arctic Oscillation index and increased activity of Rossby waves of greater amplitude. Also, it makes the occurrence of intense and prolonged blockings in middle and high latitudes more likely. With an increase in CO_2, similar changes occur mainly in the upper troposphere, while in the lower troposphere, their value is noticeably smaller. This circulation pattern is associated with an increased frequency of extreme weather events in the mid-latitude troposphere. This picture is entirely consistent with some previous studies on this issue [47,48].

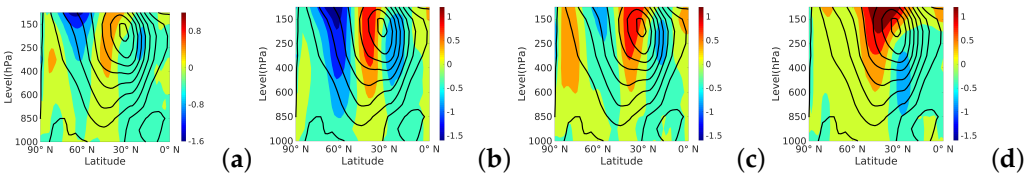

Figure 3. Anomalies of the zonal distribution of the zonal velocity component resulted from averaging the winter (December-January-February) months over the last 30-year period. The isolines show the zonal distribution in the B_0 experiment. Color shading highlights the deviations in the A_1 (**a**), A_2 (**b**), C_1 (**c**), and C_2 (**d**) experiments.

4.3. Wave activity and blockings

Wave activity, as defined by (6), is an objective measure for the spatial variation of physical properties and the essential diagnostics for the interaction of vortices and mean flow. Figures 4,5 show the anticyclonic local wave activity for the past ten years of five 100-year runs. In winter, increased wave activity is noticeable in storm tracks over the Atlantic and Pacific Oceans (Fig. 4a), corresponding to the experiment B_0. In the albedo experiments

(Figures 5a-d), the wave activity is increased over Europe and America compared to the B_0 experiment (Fig. 4a) and decreased over the Atlantic Ocean and Asia. The response of the wave activity distribution to an increase in the concentration of CO_2 (Figures 5e-h) is similar over Europe but qualitatively different elsewhere. In the C_1 experiment, the wave activity significantly increases over Asia and America, while in the C_2 experiment, the change in wave activity over America is small and becomes negative over Asia.

In summer (Figure 4b), the maximum wave activity is in the subtropical latitudes. The difference between experiments is insignificant (not shown).

Figure 5 also demonstrates the shift of wave activity in the eastern direction, which may indicate a displacement of storm trajectories to the east. Blocking phenomena often occur at the outlet of jet stream zones onto the continent, such as over the northeastern North Atlantic and the eastern Pacific (see [49]). Comparing the results shows that the decrease in wave activity over the Atlantic Ocean in the albedo experiments corresponds to a reduction in the blocking number. The area of storm trajectories over the Pacific Ocean is almost unchanged: the number of blockings and the magnitude of wave activity remains approximately at the same level. In addition, it is worth noting that all experiments demonstrate the peak of wave activity in western Europe, which also corresponds to the reanalysis data showing the predominance of anticyclonic circulation in this region [42]. In [50], it was noted that the process of blocking formation in the North Pacific Ocean might differ from that in the Euro-Atlantic sector, and that, while in the formation of North Pacific blocking, nonstationary eddies of synoptic-scale play a vital role, blocking in the Euro-Atlantic region is caused by quasi-stationary waves. Thus, these results suggest that the wave activity flux associated with stationary (or quasi-stationary) Rossby waves is of paramount importance for the blocking process over Europe. In contrast, the influence of non-stationary synoptic-scale processes is necessary for this over the North Pacific Ocean.

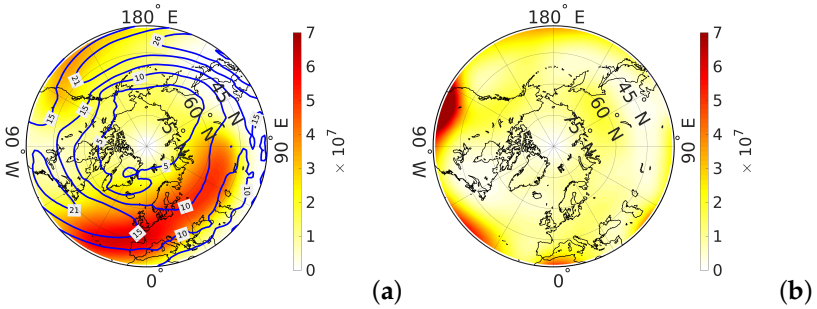

Figure 4. LWA distributions for winter with contours of of wind speed U (**a**) and summer (**b**).

Stationary waves ultimately arise from asymmetries on the Earth's surface, mountains, continent-ocean contrasts, and sea surface temperature asymmetries. Understanding strictly how stationary waves are created and maintained is a fundamental challenge in climate dynamics. Wave amplitudes in the northern hemisphere are most remarkable in winter, moderate in the transitional seasons of spring and autumn, and weakest in summer.

Stationary waves play a crucial role in block formation, but the onset of the blocking process is still poorly understood and remains a challenging problem. Due to incomplete understanding, the mechanisms of blocking formation remain somewhat subjective, and the various blocking indices are not always consistent with the impact of climate change on them.

Preprints (www.preprints.org) | NOT PEER-REVIEWED | Posted: 11 August 2021 doi:10.20944/preprints202108.0261.v1

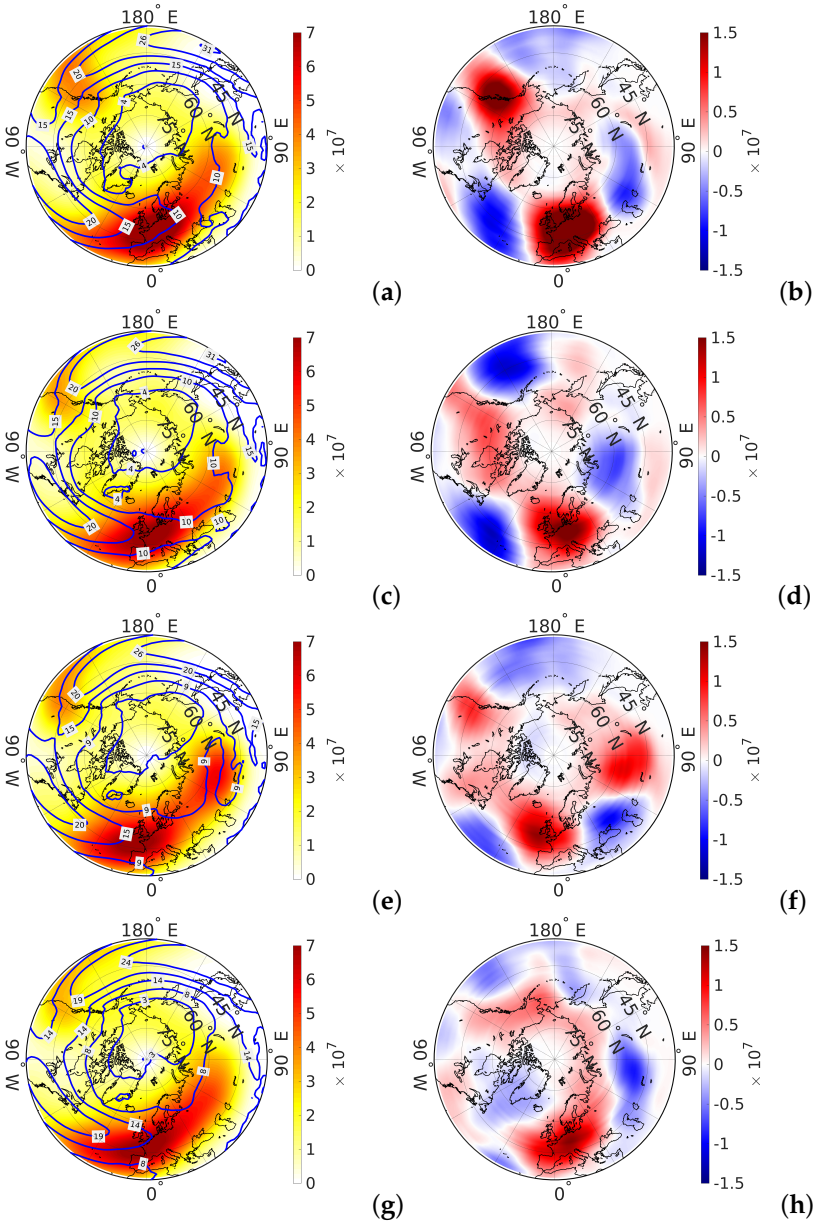

Figure 5. LWA winter distribution with countours of wind speed U: (**a**), (**b**) – A_1 and its difference with B_0; (**c**), (**d**) – A_2 and its difference with B_0; (**e**), (**f**) – C_1 and its difference with B_0; (**g**), (**h**) – C_2 and its difference with B_0.

In [49], authors considered a mechanism for atmospheric jet blocking at mid-latitudes, similar to the traffic jam problem. They suggested a local wave activity (LWA) of finite amplitude, as an estimate of potential vorticity waviness, based on the theory of interaction between waves and mean flux. It was pointed out that the relationship between LWA and block formation is based on several properties of LWA, in particular, on a quantitative assessment of the mutually compensating tendency between the meandering of the jet stream and the speed of the western stream. In our work, to assess the relationship between LWA (A_N) and U (zonal wind), we also calculated the temporal covariance field between LWA and U (both at 500 hPa) for the winter season (December-February), averaged over the last 15 years of modeling. The covariance turned out to be negative everywhere (Fig. 6a) in B_0 as well as in other experiments: that is, when the jet strongly meanders, the western flow slows down (and sometimes changes to the eastern one). The mutually compensating trends in LWA and zonal velocity are shown in the scatterplots (Figures 6b,c) in B_0 for extremal points in Atlantic and Pacific oceans shown in Figure 6a, suggesting an

approximate relationship $A_N \approx A_0 - kU$, where A_0 and k are positive constants. The red lines in Figures 6b,c are constructed by the least squares method as a best linear fit for all events. The green and blue lines are the best fit for those events, which lie above and under the red line. These lines divorce when A_N is low and gather when A_N is high. It means that dispertion of zonal velocity is higher when wave activity is low.

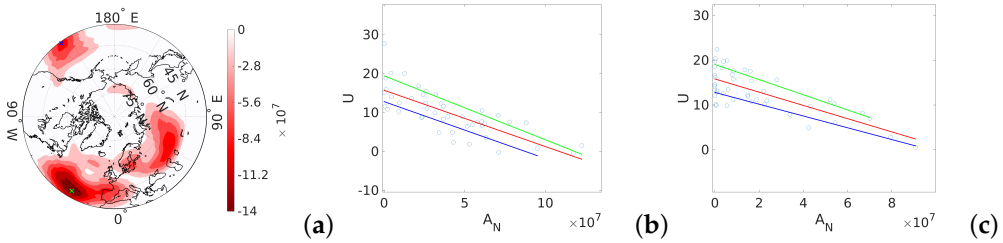

Figure 6. Covariation and scatter diagram of the average winter values of A_N (m^2) and U ($m \cdot s^{-1}$) for the last 15 years of B_0 modeling; (**a**) – covariation coefficient distribution with maximally negative values in Atlantic and Pacific oceans labelled by cross-sign, (**b**) – Scatter diagram in Atlantic extremal point, and (**c**) – Scatter diagram in Pacific extremal point. The red straight line is constructed by the least squares method for all events, the green line is for those events, which lie above the red line and the blue line is for those events, which lie under the red line.

Table 2 summerize the corresponding coordinates of extremal points in Atlantic and Pacific oceans along with the value of regression coefficient k in these points.

Table 2. Points of extremal correlation between A_N and U in Atlantic and Pacific oceans for experiments with the values of corresponding regression coefficient k in these points.

Experiment	Atlantic Ocean		Pacific Ocean	
	Coordinates	k, m·s 10^7	Coordinates	k, m·s 10^7
B_0	42N, 28W	-1.06	42N, 148W	-1.15
A_1	40.5N, 26W	-1.21	39N, 136W	-1.28
A_2	46.5N, 4W	-0.73	36N, 178W	-3.8
C_1	45N, 12W	-0.99	37.5N, 122W	-0.94
C_2	45N, 18W	-1.37	36N, 162W	-2.44

Figures 7, 8, and 9 show the blocking rate in terms of the number of blocking events defined according to criterion (7) and (8) over the last ten years of the experiment.

In winter (December-February), the conditions for the formation of blockages most often occur around the pole, on average being limited to latitude 60°N, but at the same time reaching central Europe, the southern Urals, and Kazakhstan (Fig. 7a). The highest frequency, in this case, falls on the territory of Yakutia and the Chukchi Sea, reaching 15 blockages for all winters of 10 years (i.e., on average, 1.5 blockings per winter). Also, blockages are frequent in Greenland, the Norwegian Sea, and Kazakhstan - up to 5-10 events. We can also note the probability of blocking in the North Pacific and Atlantic Ocean (2-3 events) along storm tracks.

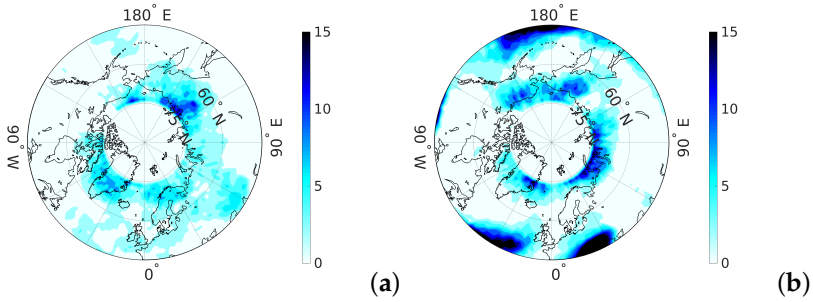

Figure 7. Climatology of blocking frequency in winter (**a**) and in summer (**b**).

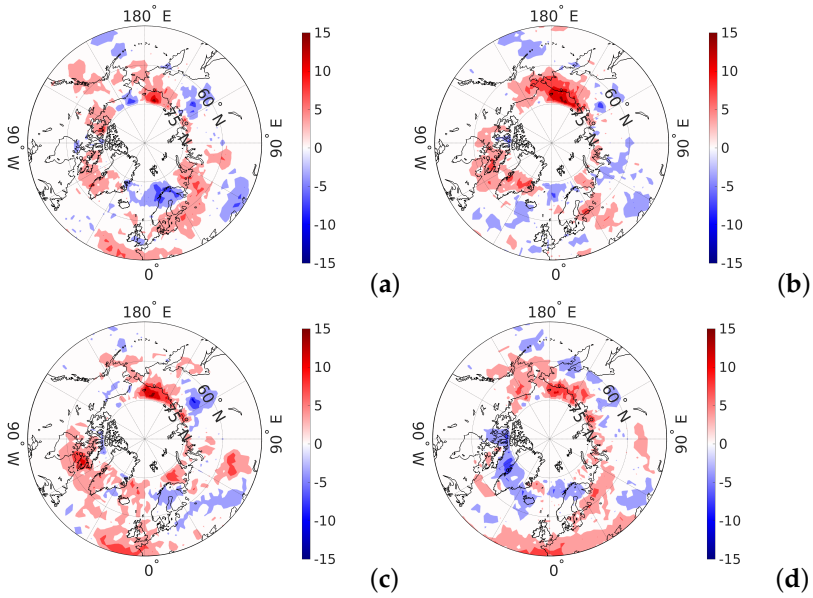

Figure 8. Climatology trends of blocking frequency in winter: (**a**) – difference between A_1 and B_0, (**b**) – difference between A_2 and B_0, (**c**) – difference between C_1 and B_0, (**d**) – difference between C_2 and B_0

In the case of an increase in CO_2 concentration to 450 ppm in experiment C_1 (Fig. 8c), when the decrease in the ice field is slight, the number of blockages increases by 10-15 events in the region of the East Siberian Sea and the Canadian Arctic Archipelago (CAA), by 5-10 events in the north-western Atlantic, the south of the Barents Sea, Kazakhstan and the south of western Siberia. At the same time, it decreases noticeably (by 5-10 events) in Yakutia and Eastern Europe. With an even more significant increase in CO_2 concentration in the C_2 experiment (Fig. 8d), a belt of positive change in the blocking frequency is formed, extending from Europe and the adjacent part of the Atlantic and further along the Arctic coast of Eurasia to Alaska. In this case, the CAA region falls into the zone of reducing the number of blockings. The reduction of the ice field in the A_1 experiment is approximately the same as in the C_2 experiment. Therefore, the tendencies in blocking frequency (Fig. 8a) almost entirely coincide with experiment C_2, except for CAA. In contrast to C_2, the number of blockings increases by 5-10 events here. With an even greater decrease in albedo in A_2 and a significant reduction in ice, the picture of the change in the blocking conditions in A_2 looks more different (Fig. 8b). In almost the entire ring in the region of 65-70°N, the number of blockages increases by 5-15 events, including CAA. An exception is the Norwegian and Greenland Seas region, where a decrease of about 5 events can be noted, as for the central regions of the North Atlantic. The exact change is seen for the south and north of eastern Europe, the south of eastern Siberia, and the central part of the Pacific Ocean.

Thus, the general features of changes in the blocking conditions are 1) an increase in the number of blockages in the region of the East Siberian and Chukchi Seas, including

Alaska; 2) the growth of blocking number in central and eastern Europe; 3) reducing the number of blockages in the area of northern Scandinavia and the Norwegian Sea; 4) decrease in the Caspian region and Kazakhstan; 5) decrease in the region of Yakutia. The CAA region demonstrates an ambiguous change in the blocking frequency: an increase in experiments C_1, A_1, and A_2, and a decrease in experiment C_2. The difference can be attributed to the peculiarities of one or another method of ice reduction in numerical experiments and the nonlinearity of the climate system's response to disturbances.

Summer (June-August) blocking frequency distribution for the base experiment B_0 is shown in Figure 7b. The areas with the most frequent blockages can be divided into two rings. The first is located near the pole at a latitude of approximately 65-70°N and roughly corresponds to the position of the coastline bordering the Arctic Ocean. Three zones with the highest frequency of blocking events can be distinguished here: in the Barents-Kara-Laptev seas, on the Arctic coast of Chukotka and Alaska, and the Greenland region. These are blockings occurring on the northern flank of the jet stream. The second ring adjoins the subtropics and corresponds to the blockings forming on the southern flank. In subtropical latitudes, the number of blockings is much greater in summer when anticyclonic vorticity prevails. The most significant number of blocking events can be noted in the North Atlantic and North Pacific regions along storm tracks and the western parts of Europe and America, where they hits the continent. At the same time, vast areas of Central Asia are found to be on the sidelines of these events.

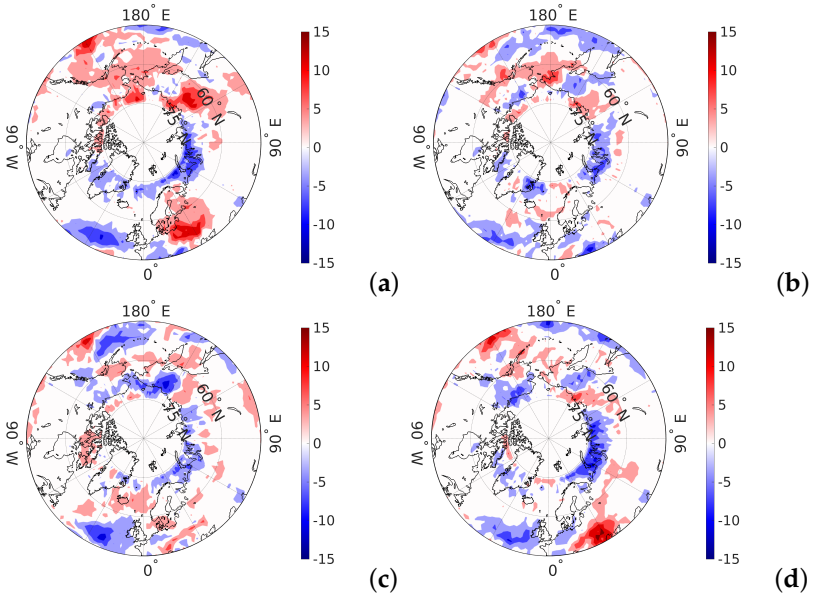

Figure 9. Climatology trends of blocking frequency in summer: (**a**) – difference between A_1 and B_0, (**b**) – difference between A_2 and B_0, (**c**) – difference between C_1 and B_0, (**d**) – difference between C_2 and B_0

With a decrease in albedo in the A_1 and A_2 experiments within the first ring (Fig. 9a,b), the blocking frequency noticeably decreases on the line of the Barents-Kara-Laptev seas, but at the same time, it strongly increases to the east of it in the Yakutia region. The blockage rate also increases in the second area, covering the entire Bering Sea. The probable cause of this increase is the growth of wave activity due to a decrease in the gradient. However the blockage rate decreases in the Greenland region. In the second ring, a noticeable increase in frequency in the A_1 experiment, when the reduction of the ice field is less significant, takes place in northeastern Europe and the northeastern part of the Pacific Ocean. In the Atlantic, the number of blockages is decreasing. With a significant reduction in the ice field in the A_2 experiment, these changes are less pronounced, but the frequency decreases noticeably in the central part of the Pacific Ocean.

The changes are similar with an increase in CO_2 in the first ring (Fig. 9c,d). However, in the region of Chukotka and Alaska in the C_1 experiment, there is a slight decrease in the blocking frequency, and in the C_2 experiment, the distribution of trends in this area is spotty and close to neutral. The second ring also shows an increase in blockages in eastern Europe and the northeast Pacific and a decrease in the North Atlantic. Thus, except for the region of Chukotka and Alaska, the summer trends of the A_1 and A_2 experiments coincide with the C_1 and C_2 trends. This fact allows us to assume that the indicated tendencies are caused precisely by the reduction of the Arctic ice. We can also assume that with a slight increase in the concentration of CO_2 (C_1), when the ice field changes insignificantly, the trend in the frequency of blockages in the region of Chukotka and Alaska is negative. However, with a further increase in the CO_2 concentration (C_2), when the decrease in Arctic ice becomes more significant, an opposite trend is activated in this area, similar to experiments A_1 and A_2, which eventually compensates for the previous trend.

Along with the blocking frequency, an essential characteristic of this phenomenon is its intensity. The blocking intensity depends on the relative elevation of the maximum of the geopotential height. As before, we will use the z_{500} characteristic. If we assume an Ω-type blocking structure, then the line connecting two adjacent minima of z_{500} at the midpoint will have $z = (Z_u + Z_d)/2$, where Z_u and Z_d are z_{500} values at the upstream and downstream minimum points. Then the elevation of the maximum above this line can be estimated by taking the difference $Z_{\max} - z$. If we take the ratio of this value with the average $(Z_{\max} + z)/2$, then we get the relative elevation. When we are dealing with Rex-type blocking, one of the lows can be far away. Therefore, one can take the z_{500} value at a certain distance from the high. The very idea underlies the BI blocking intensity index proposed in [51]. For each coordinate point (λ, ϕ) where a blocking event is detected according to (7), we define BI as

$$BI(\lambda, \phi) = 100\% \frac{-Z_u + 2Z - Z_d}{Z_u + 2Z + Z_d}, \tag{9}$$

where $Z = z_{500}(\lambda, \phi)$ and Z_u and Z_d are the minimum values of the z_{500} field within $\lambda \pm 60^\circ$ upstream and downstream at ϕ latitude.

In the expression (9), if we assume that $Z_u = Z_d = \bar{Z}(1 - \alpha)$ and $Z = \bar{Z}(1 + \alpha)$, then we get that $BI = 100\% \alpha$. Thus, we can interpret the BI value as the amplitude of the sawtooth change in the geopotential height in the blocking region. Approximately the same we can say about pressure, so the pressure drop in the blocking area will equal $p = 500 \cdot (1 \pm \alpha) = 500 \cdot (100\% \pm BI)$ hPa. By definition, BI is always positive. The higher BI index means the greater blocking intensity. If at some point $BI = 0$, then there is no blocking.

Figure 10 demonstrates the distribution of the average blocking intensity obtained over the last ten years of the B_0 100-year experiment separately for winter (December-February) and summer (June-August). Comparing this figure with the blocking frequency figure 7, we can see that they are almost negatives of each other. That is, the more frequent the blockings, the less intense they are and vice versa.

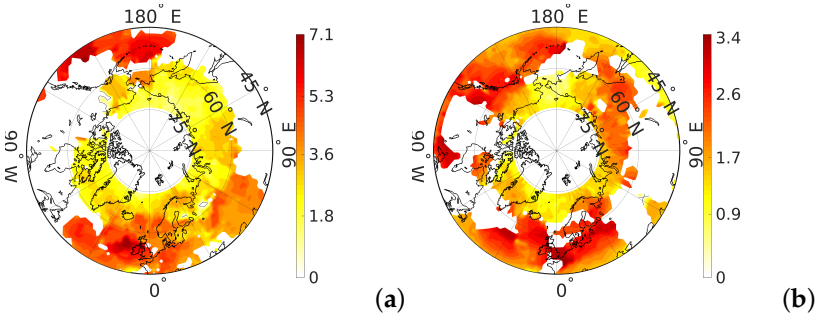

Figure 10. The blocking intensity index BI in the B_0 experiment averaged over the last 10 years of 100-year run: (**a**) – in winter (December-February), and (**b**) – in summer (June-August).

Preprints (www.preprints.org) | NOT PEER-REVIEWED | Posted: 11 August 2021 doi:10.20944/preprints202108.0261.v1

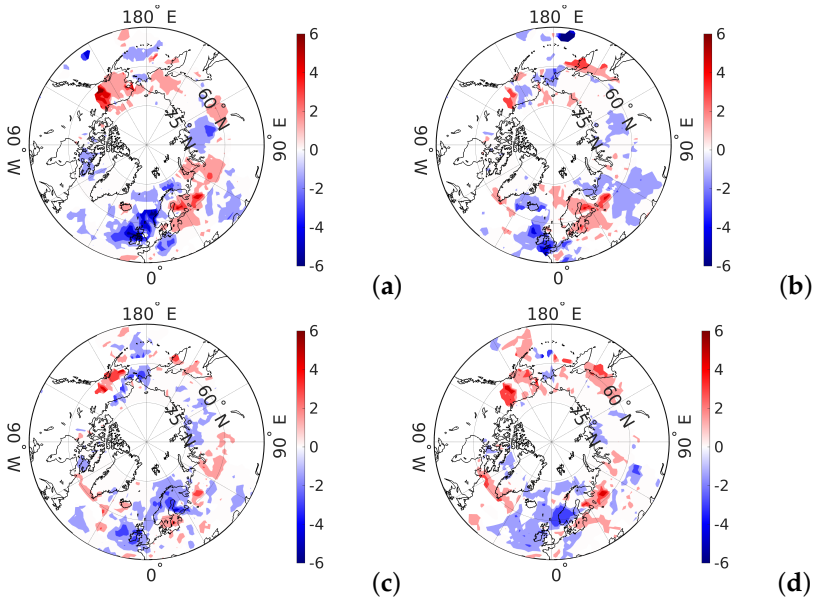

Figure 11. The winter blocking intensity index BI averaged over the last 10 years of 100-year run: (**a**) – difference between A_1 and B_0, (**b**) – difference between A_2 and B_0, (**c**) – difference between C_1 and B_0, (**d**) – difference between C_2 and B_0.

We note that in winter (Figures 7a, 10a) the most intense blockings are $BI \approx 7\%$ with pressure drops at an altitude of 5.5 km (approximately corresponds to z_{500}) about 500±35 hPa are formed in the eastern part of the Pacific Ocean. However, during the ten years under consideration, these events occurred only 1-2 times. Blockings of the same intensity occur in the eastern Atlantic near the British Isles, but these events happen 2-3 times more often. The Ural blocking, which forms approximately at the longitude of the Ural Mountains, corresponds to BI ≈2-4% and occurs about once every 1-2 years. Roughly the same picture for the blocking in the Greenland region. For areas with the maximum frequency of blockings (Yakutia and the Chukchi Sea), their intensity is only 1-2%. Figure 11 shows trends associated with changes in blocking intensity in experiments A_1, A_2, C_1 and C_2. We can note that the results of almost all experiments indicate a decrease in the intensity of blockings near the British Isles by 3-6% and an increase by the same 3-6% in northeastern Europe. We can interpret these changes as a displacement of the center of intensity to the east and increased Ural blocking. Based on the analysis of the results of six experiments using different climatic models [52] noted an increase in the Siberian maximum and a weakening of the Icelandic minimum, both changes are going along with strengthening the Ural blocking and decline of blocking intensity in the western part of the North Atlantic. On the other side of the Arctic, the intensity of blockings is increasing in Alaska and the Sea of Okhotsk, which is also supported by [52] finding of the Aleutian Low strengthening.

In summer (Figures 7b, 10b) the intensity of blocking decreases and the maximum value is only 3.4% (ie 500±17 hPa). Such blockings are formed at a latitude of approximately 50-55°N. Note that, as a rule, the places of their formation are located at the edge of the zones of the highest frequency (Figures 7b), namely in the Aleutian Islands, southern Alaska and British Columbia, American Lakes, the central part of the North Atlantic, central and eastern Europe. These events occur about 2-3 times every ten years. We can note less intense (2.5-3%) blockings with the same frequency in the east of Asia near the Sea of Okhotsk. More frequent blockings that form along the Arctic coast are even less intense, and their BI index is only 1-2%.

The most significant increase in the intensity of blocking in summer by 1-2% (Figure 12) in the experiments A_1, A_2, C_1 and C_2 we can note in the area of the Greenland, Norwegian, and Barents seas, and also near the Bering Strait and the Chukchi Sea, i.e., in places directly

Preprints (www.preprints.org) | NOT PEER-REVIEWED | Posted: 11 August 2021 doi:10.20944/preprints202108.0261.v1

related to the retreat of the ice field. At the same time, a decrease in intensity by about 1% in the CAA region and Yakutia can be noted.

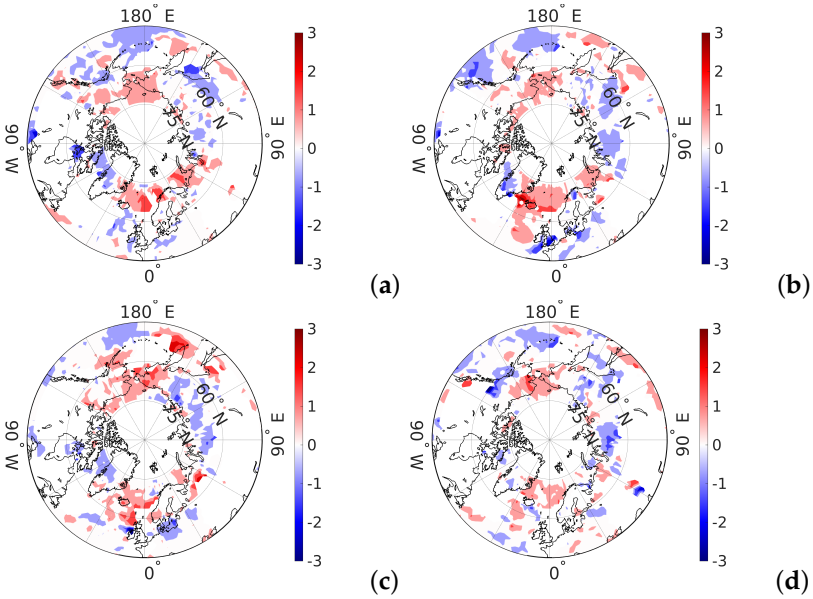

Figure 12. The summer blocking intensity index BI averaged over the last 10 years of 100-year run: (**a**) – difference between A_1 and B_0, (**b**) – difference between A_2 and B_0, (**c**) – difference between C_1 and B_0, (**d**) – difference between C_2 and B_0.

5. Discussion

In the experiments with decreased albedo, the zonal wind speed decreases near 55-60°N. A weakening of the polar potential vorticity gradient in the lower stratosphere near the tropopause goes along with this speed reduction. Also, in subtropics, the zonal wind increases. In this case, the meandering of the jet flow grows, which can be measured by the value of LWA. Persistent high LWA values may indicate a high probability of blockage in the atmosphere. Jet blocking is an anomalous weather event, so it is not surprising that high LWA values are associated with geopotential height anomalies. Thus, understanding the current distributions and what factors might affect the LWA values can provide insight into extreme weather conditions. In addition, insights are emerging on how climate change can affect atmospheric dynamics at mid-latitudes. For blocking to occur, the LWA values must exceed the wave break threshold.

Typically, the geopotential height increases with the anticyclonic LWA and decreases with the cyclonic LWA. Since the anticyclonic LWA is higher than the cyclonic LWA, this increases the geopotential height with the LWA in most locations.

In the case of a decrease in albedo, the LWA distributions change significantly with an increase in wind shear in the stratosphere (Figure 3). As the wind shear increases, the LWA values increase. This result is quite reasonable given that an increase in wind shear leads to a rise in eddy activity caused by growing baroclinic instability and an increase in the LWA values and blocking frequency.

The system for diagnostics of local wave activity (LWA) of finite-amplitude allows one to quantify the interaction of mean vortex flows on a regional scale.

In the Northern Hemisphere, storm tracks generally run in the Pacific and Atlantic sectors. Surface orography contributes to the difference in spatial structures of storm trajectories through stationary Rossby waves [53–55].

Storm tracks are usually more active in winter than in summer when pole-equator and continent-ocean temperature gradients increase baroclinicity. However, the suppression of storm activity in the North Pacific in midwinter is a notable exception [56].

In both storm track regions, poleward heat flux at the lower levels is the primary source of LWA. However, the compensating mechanisms are different.

Simulation data show that LWA and zonal wind have negative covariance in the Atlantic and over the Pacific. This fact suggests that the blocking maxima occur near the stationary high-pressure anomalies at the exit of the storm track region.

While there is no universally accepted definition of blocking, most researchers today identify them as ridges in a jet stream that persist for five days or more. Today, the inversion of the z_{500} geopotential height gradient and the potential vortex at mid-latitudes are most often used to identify blocking events. This work used the first of these identification methods. However, it is worth noting that since the models have their drawbacks, they cannot describe some aspects of the physics of the process associated with the life cycle of blocking development, including large-scale interactions.

One of the known problems associated with blocking is its substantial natural variability, including, for example, a small number of rare but persistent and significant events. This variability has several practical implications. For example, it often takes long periods or several members of the modeling ensemble to get good blocking statistics. Given the level of natural variability, it is possible that observations have not yet revealed any entirely consistent long-term trends in blocking. Considering the importance of natural variability for mid-latitude circulation in general (e.g.,[57]), it is likely that it will continue to play a leading role in blocking change over the next few decades.

Determining the blocking itself has become a significant problem because different lock indices target different block characteristics. Blocking has always been a problem for weather forecasts and climate models because of its specific nature, which is difficult to simulate correctly numerically [40]. Several generations of climate models have shown significant negative deviations in blocking frequency, especially in the European sector (e.g., [20]). However, there is general agreement that blocking rates should decrease in the next century [20], but this may depend on the index used. Moreover, observations can hardly confirm any trend [31,42].

Choosing a lock index is a necessary and fundamental step for this job. There are indices based on flow topology and determined through model or observed meridional gradients of the geopotential or potential vortex (e.g., [23,40]) that we use in our work, but there are other types of indices (e.g., [20,30].

Atmospheric blockages in the northern hemisphere in winter and summer were analyzed in a climate model intercomparison project. Data from CMIP5 (2012) and CMIP6 (2019) were compared with different reanalysis datasets. This vast dataset provided insights into the ability of general circulation models to reproduce atmospheric blocking in today's climate and evaluate it in future scenarios [58]

In general, blocking can be characterized as a persistent but successfully resolved, serious problem of climate modeling. Although the most recent generation of models (e.g., CMIP6) still exhibits significant errors in blocking rates in critical regions. The efforts of the modelers have resulted in significant improvements that, on average, have halved the blocking errors experienced by earlier generation models, for example, by increasing the resolution.

The analysis of the blocking intensity showed that in the experiments, as a result of the reduction of the Arctic ice, the intensity maximum near the British Isles shifts to the east, thereby strengthening the winter Ural blockings by 3-6%. In [59] authors examined the relationship among Ural blocking, and the background conditions associated with Arctic warming over the Barents and Kara Seas and found that the intensity of Ural blocking is significantly related to this warming. In winter, the intensity of blockings in the Alaska region and the Sea of Okhotsk also increases. In summer, the changes in intensity are not so significant, about 1%, and mainly concern the areas affected by ice retreat.

Comparing blocking frequency and blocking intensity shows that the more frequent the blockings, the less intense they are. In this respect, it is interesting to consider the field built as the product of the last two. It will give us an idea of where the transitions of wave energy into blocking energy occur.

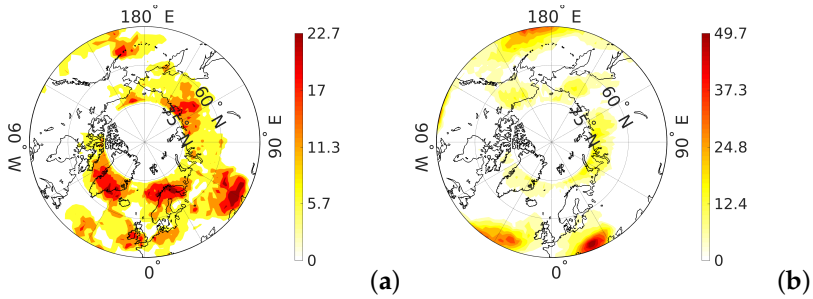

Figure 13. The blocking intensity index BI in the B_0 experiment Figure 10 multiplied by blocking frequency Figure 7: (**a**) – winter (December-February), and (**b**) – summer (June-August).

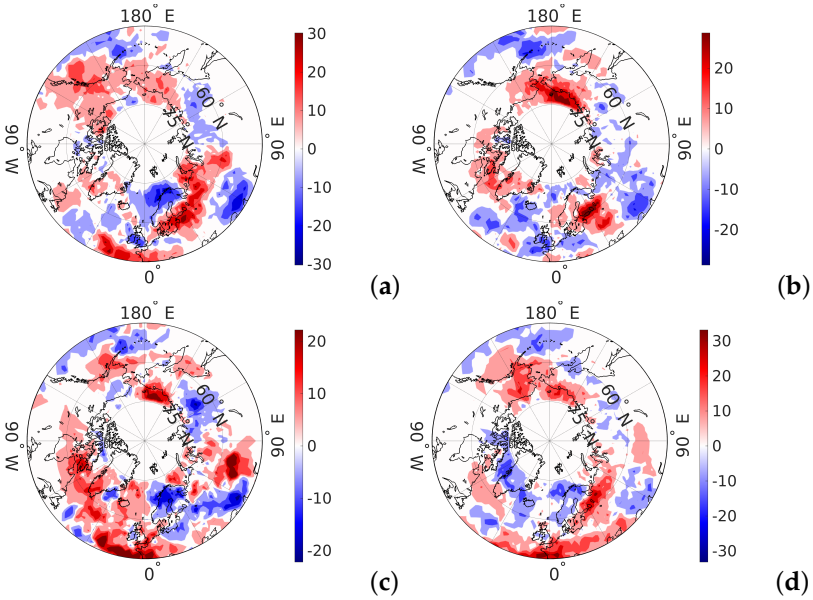

Figure 14. The winter blocking intensity index BI multiplied by blocking frequency: (**a**) – difference between A_1 and B_0, (**b**) – difference between A_2 and B_0, (**c**) – difference between C_1 and B_0, (**d**) – difference between C_2 and B_0.

Figure 13a shows that such energy transformations are carried out in the following regions: northern Scandinavia, Yakutia, the Chukchi Sea, Greenland, eastern Aleutian Islands, the British Isles region, and Kazakhstan. Moreover, in the first four regions, blockings are more frequent but less intense. In the rest, on the contrary, blockings are higher in intensity but occur less frequently.

In experiments with the reduction of Arctic ice (Fig. 14), we can identify the following general tendencies: weakening of processes in the vicinity of the British Isles and Kazakhstan, with a simultaneous increase in northern Europe and the Urals; weakening in the east of the Aleutian Islands and strengthening in the region of Alaska and the Sea of Okhotsk. All the tendencies noted are associated with an increase in energy of blockings in the northern areas, with a simultaneous decrease of the southern ones.

In summer (Fig. 13b), in addition to the regions adjacent to the subtropics in the central part of the Pacific and the Atlantic Ocean and southern Europe, the Arctic part can also be distinguished: the line of the Barents-Kara-Laptev Seas, the Kolyma basin, and northern Alaska. As a result of ice reduction in Figure 15, one can distinguish the following summer trends: weakening in the areas mentioned above close to the subtropics, weakening along the line of the Barents-Kara-Laptev Seas, strengthening in the Bering and Chukchi Seas. There are ambiguous trends in the Greenland and Norwegian Seas, in the Beaufort Sea, in the Kolyma basin. In Eastern Europe, the growth is mainly, but with 75% of ice mass lost in A_2, it becomes insignificant.

Preprints (www.preprints.org) | NOT PEER-REVIEWED | Posted: 11 August 2021 doi:10.20944/preprints202108.0261.v1

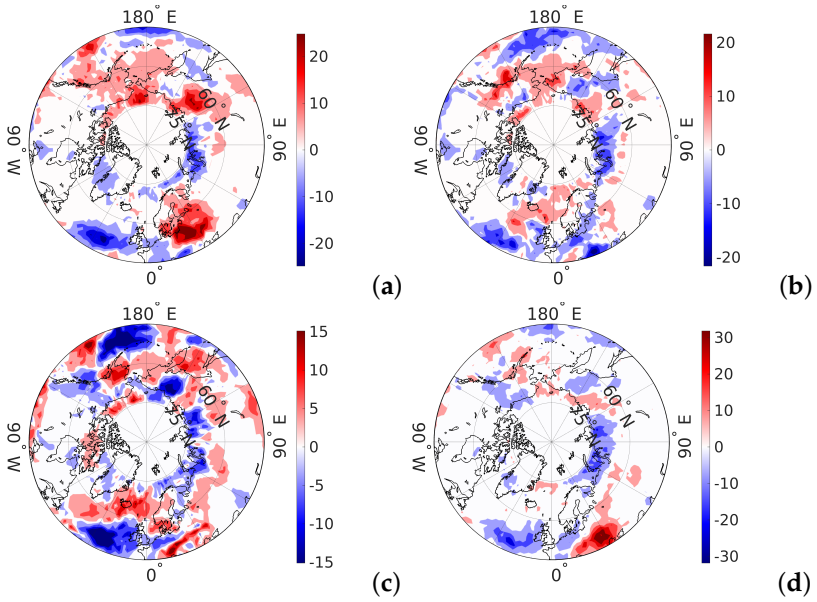

Figure 15. The summer blocking intensity index BI multiplied by blocking frequency: (**a**) – difference between A_1 and B_0, (**b**) – difference between A_2 and B_0, (**c**) – difference between C_1 and B_0, (**d**) – difference between C_2 and B_0.

Comparing the results of the action of two mechanisms (experiments A_1-A_2 and C_1-C_2), leading to a decrease in Arctic ice, one can see certain similarities and differences. With an increase in the concentration of CO_2 in the atmosphere and melting of ice as a result of this increase, the effective albedo of the underlying surface in the Arctic inevitably decreases, since leads and melt ponds appear, and the snow surface becomes darker due to an increase in water content. Therefore, experiments C_1 and C_2 have features in common with experiments A_1 and A_2, which are associated with ice reduction. However, in addition to this, an increase in CO_2 concentration entails, as can be seen from Table 1, significant heating of atmospheric air, and the unevenness of this heating further sharpens or smooths out the zonal gradients, and this is no longer associated with a decrease in the amount of ice. Therefore, analyzing the results of experiments C_1 and C_2, we cannot attribute the consequences exclusively to changes in the ice. Experiments A_1 and A_2 with an artificial decrease in albedo also have several consequences not related to changes in ice, since here the natural radiation balance on the surface is disturbed, as a result of which, as again follows from Table 1, one can also note an increase in the surface air temperature, although not so significant as in experiments C_1 and C_2. Other consequences are also possible, which are difficult to predict in advance.

Analyzing the similar features of the resulting distributions, we can assume that they result from ice reduction, which we would like to obtain. However, they can also result from increased air temperature or other common consequences for the two mechanisms. If an increase in temperature causes the similarity of the consequences, their manifestations in experiments C_1 and C_2 would be brighter since the increase in temperature is more significant in these experiments. However, as we can see from the presented results, this is far from the case. Therefore, we tend to attribute the similar features to the effects of ice reduction. Nevertheless, it is not possible to unequivocally prove this, so we can only talk about the possibility of such interconnections. Based on this, we can assume that the following changes in the atmosphere and its dynamics are associated with the reduction of ice in the Arctic:

1. Increase in tropospheric temperature at latitude 60-70°N, and a decrease in stratospheric temperature at latitude 40-50°N, both cause a reduction in the gradient at the tropopause level in mid-latitudes. An increase in the temperature of the upper tropo-

sphere at latitude 20-30°N, and consequent increase in the gradient at the tropopause level at latitudes 30-40°N (Fig. 2);
2. Acceleration of the zonal flow at latitude 30-50°N, decelerating the flow at latitude 20-30°N. It means a shift of the jet to the north. Acceleration of eastern transport at latitude 80°N (Fig. 3);
3. Intensification of wave activity in Europe, Western America, and Chukotka, its weakening in the south of Siberia and Kazakhstan (Fig. 5);
4. Winter increase in the number of blockings in the East Siberian and Chukchi Seas, including Alaska, in central and eastern Europe and the reduction in blockings in the Norwegian Sea, Caspian region and Kazakhstan, and in Yakutia (Fig. 8);
5. Summer decrease in the number of blockings on the line of the Barents-Kara-Laptev seas, in the Greenland region, in the central Atlantic and Pacific Oceans, but increase in the Yakutia, in northeastern Europe and the northeastern part of the Pacific Ocean (Fig. 9).

In addition to the similar features resulted from the A1-A2 and C1-C2 experiments, there are significant differences that also make sense to list:

1. With minor changes in albedo, an increase in the polar stratospheric temperature (> 1°C), and with a significant increase in CO_2 concentration, its decrease (1°C);
2. The temperature rise at the border of the troposphere and stratosphere in the tropics takes place only with an increase in the concentration of CO_2;
3. The deceleration of the flow at latitude 50-65°N occurs only with a decrease in albedo and disappears with an increase in CO_2;
4. Weakening of wave activity in the central part of the oceans in A_1. Weakening in the northwestern part of the oceans in C_2, while in A_1, there is an increase.
5. Winter increase in the number of blockings occurs in CAA in experiments C_1, A_1, and A_2, while in experiment C_2 number of blockings decreases;
6. Summer increase in the number of blockings occurs in the entire Bering Sea in A_1 and A_2, while in the C_1 there is a slight decrease in the blocking frequency, and in the C_2 there is no significant trend.

If we talk about an increase in CO_2 concentration as the main factor causing recent climatic changes, then the differences indicate the processes in the atmosphere, which are (most likely) directly caused by an increase in the amount of CO_2 in the air and are not associated with changes in the ice field.

6. Conclusions

This paper considers a series of numerical experiments to identify the direct role of the Arctic sea ice reduction process in establishing trends in the northern atmosphere circulation. Aimed at this, we used two mechanisms of ice reduction: an increase in the concentration of carbon dioxide in the atmosphere, and a reduction in the reflectivity of ice and snow. The most prominent consequences of ice reduction, as a result of numerical tests, were the weakening of temperature gradient at the tropopause level in mid-latitudes, the zonal wind speed decrease near 50-60°N and its increase in the subtropics, intensification of wave activity in Europe, Western America, and Chukotka, and its weakening in the south of Siberia and Kazakhstan. Changes in wave activity lead to changes in the frequency and intensity of blockings. We used a modified blocking criterium to evaluate the simulated blocking frequency and blocking intensity for north hemisphere mid-latitude regions in winter and summer, corresponding to ice reduction. In experiments with the reduction of Arctic ice, we can identify the following general tendencies associated with winter blockings: their weakening in the vicinity of the British Isles and Kazakhstan, with a simultaneous increase in northern Europe and the Urals; weakening in the east of the Aleutian Islands and strengthening in the region of Alaska and the Sea of Okhotsk. These tendencies mean an increase in energy of blockings in the northern areas, with a simultaneous decrease of the southern ones. The summer trends include weakening in areas

close to the subtropics, weakening along the Barents-Kara-Laptev Seas, strengthening in the Bering and Chukchi Seas. Also, blockings strengthen in Eastern Europe, but extreme ice loss makes this strengthening insignificant.

Author Contributions: Conceptualization, G.P. and V.K.; methodology, V.K.; software, E.V.; formal analysis, V.G. and I.B.; investigation, G.P.; writing—original draft preparation, G.P.; writing—review and editing, G.P.; visualization, V.G.; project administration, G.P.; funding acquisition, G.P. All authors have read and agreed to the published version of the manuscript.

Funding: This research was funded by Russian Science Foundation grant number 19-17-00154.

Institutional Review Board Statement: Not applicable.

Informed Consent Statement: Not applicable.

Acknowledgments: The Siberian Branch of the Russian Academy of Sciences (SB RAS) Siberian Supercomputer Center is gratefully acknowledged for providing supercomputer facilities.

Conflicts of Interest: The authors declare no conflict of interest. The funders had no role in the design of the study; in the collection, analyses, or interpretation of data; in the writing of the manuscript, or in the decision to publish the results.

References

1. Volodin, E.M.; Mortikov, E.V.; Kostrykin, S.V.; Galin, V.Ya.; Lykossov, V.N.; Gritsun, A.S.; Diansky, N.A.; Gusev, A.V.; Iakovlev, N.G.; Shestakova, A.A.; Emelina, S.V. Simulation of the modern climate using the INM-CM48 climate model. *Russian Journal of Numerical Analysis and Mathematical Modelling* **2018**, *33*, 367–374. doi: 10.1515/rnam-2018-0032
2. Wills, R.C.J.; White, R.H.; Levine, X.J. Northern Hemisphere Stationary Waves in a Changing Climate. *Curr Clim Change Rep.*, **2019**, *5*, 372–389. doi:10.1007/s40641-019-00147-6
3. Wu, B.; Handorf, D.; Dethloff, K.; Rinke, A.; Hu, A. Winter Weather Patterns over Northern Eurasia and Arctic Sea Ice Loss. *Monthly Weather Review* **2013**, *141*, 3786–3800. doi:10.1175/MWR-D-13-00046.1
4. McIntyre, M. E.; Palmer, T. N. Breaking planetary waves in the stratosphere. *Nature* **1983**, *305*, 593–600. doi:10.1038/305593a0
5. Polvani, L. M.; Saravanan, R. The Three-Dimensional Structure of Breaking Rossby Waves in the Polar Wintertime Stratosphere. *Journal of the Atmospheric Sciences* **2000**, *57*, 3663–3685. doi:10.1175/1520-0469(2000)057<3663:TTDSOB>2.0.CO;2
6. Kim, B.M.; Son, S.W.; Min, S.K.; Jeong, J.H.; Kim, S.J.; Zhang, X.; Shim, T.; Yoon, J.H. Weakening of the stratospheric polar vortex by Arctic sea-ice loss. *Nat Commun* **2014**, *5*, 4646. doi:10.1038/ncomms5646
7. Strong, C.; Magnusdottir, G.; Stern, H. Observed feedback between winter sea ice and the North Atlantic Oscillation. *J. Clim.* **2009**, *22*, 6021–6032. doi: 10.1175/2009JCLI3100.1
8. Deser, C.; Tomas, R.; Alexander, M.; Lawrence, D. The seasonal atmospheric response to projected Arctic sea ice loss in the late twenty-first century. *J. Clim.* **2010**, *23*, 333–351. doi: 10.1175/2009JCLI3053.1
9. Sévellec, F.; Fedorov, A.; Liu, W. Arctic sea-ice decline weakens the Atlantic Meridional Overturning Circulation. *Nature Clim Change* **2017**, *7*, 604–610. doi: 10.1038/nclimate3353
10. Drijfhout, S. Competition between global warming and an abrupt collapse of the AMOC in Earth's energy imbalance. *Sci Rep* **2015**, *5*, 14877. doi: 10.1038/srep14877
11. Zhang, R.; Sutton, R.; Danabasoglu, G.; Kwon, Y.-O.; Marsh, R.; Yeager, S. G. et al. A review of the role of the Atlantic Meridional Overturning Circulation in Atlantic Multidecadal Variability and associated climate impacts. *Reviews of Geophysics* **2019**, *57*, 316–375. doi: 10.1029/2019RG000644
12. Posselt, D. J.; Heever, S. V. D.; Stephens, G.; Igel, M. R. Changes in the Interaction between Tropical Convection, Radiation, and the Large-Scale Circulation in a Warming Environment. *J. Clim.* **2012**, *25*, 557–571. doi: 10.1175/2011JCLI4167.1
13. Maykut, G. A.; Untersteiner, N. Some results from a time dependent, thermodynamic model of sea ice. *J. Geophys. Res.* **1971**, *76*, 1550–1575. doi: 10.1029/JC076i006p01550
14. Curry, J. A.; Schramm, J. L.; Ebert, E. E. Sea ice-albedo climate feedback mechanism. *J. Clim.* **1995**, *8*, 240–247. doi: 10.1175/1520-0442(1995)008<0240:SIACFM>2.0.CO;2
15. Chripko, S.; Msadek, R.; Sanchez-Gomez, E.; Terray, L.; Bessières, L.; Moine, M. Impact of Reduced Arctic Sea Ice on Northern Hemisphere Climate and Weather in Autumn and Winter. *Journal of Climate* **2021**, *34*, 5847–5867. doi: 10.1175/JCLI-D-20-0515.1
16. Huang, C.S.Y.; Nakamura, N. Local Finite-Amplitude Wave Activity as a Diagnostic of Anomalous Weather Events. *J. Atmos. Sci.* **2016**, *73*, 211–229. doi: 10.1175/JAS-D-15-0194.1
17. Rex, D. Blocking action in the middle troposphere and its effect upon regional climate: I. An aerological study of blocking action. *Tellus* **1950**, *2*, 196–211. doi: 10.3402/tellusa.v2i3.8546
18. Green, J. The weather during July 1976: Some dynamical considerations of the drought. *Weather* **1977**, *32*, 120–126. doi: 10.1002/j.1477-8696.1977.tb04532.x

19. Hoskins, B. J.; James, I. N. Fluid dynamics of the mid-latitude atmosphere. John Wiley & Sons, Ltd, The Atrium, Southern Gate, Chichester, West Sussex, PO19 8SQ, UK, 2014; 337–360. doi: 10.1002/9781118526002
20. Woollings, T.; Barriopedro, D.; Methven, J.; Son, S.-W.; Martius, O.; Harvey, B.; Sillmann, J.; Lupo, A. R.; Seneviratne, S. Blocking and its response to climate change. *Current Climate Change Reports* **2018**, *4*, 287–300. doi: 10.1007/s40641-018-0108-z
21. Chan, P.-W.; Hassanzadeh, P.; Kuang, Z. Evaluating indices of blocking anticyclones in terms of their linear relations with surface hot extremes. *Geophysical Research Letters* **2019**, *46*, 4904–4912. doi: 10.1029/2019GL083307
22. Colucci, S. J. Planetary-scale preconditioning for the onset of blocking. *J. Atmos. Sci.* **2001**, *58*, 933–942. doi: 10.1175/1520-0469(2001)058<0933:PSPFTO>2.0.CO;2
23. Pelly, J. L.; Hoskins, B. J. How well does the ECMWF ensemble prediction system predict blocking? *Quart. J. Roy. Meteor. Soc.* **2003**, *129*, 1683–1702. doi: 10.1256/qj.01.173
24. Jia, X.; Yang, S.; Song, W.; He, B. Prediction of wintertime Northern Hemisphere blocking by the NCEP Climate Forecast System. *J. Meteor. Res.* **2014**, *28*, 76–90. doi: 10.1007/s13351-014-3085-8
25. Shutts, G. The propagation of eddies in different jetstreams: Eddy vorticity forcing of 'blocking' flow fields. *Quart. J. Roy. Meteor. Soc.* **1983**, *109*, 737–761. doi: 10.1002/qj.49710946204
26. Trenberth, K. An assessment of the impact of transient eddies on the zonal flow during a blocking episode using localized Eliassen–Palm flux diagnostics. *J. Atmos. Sci.* **1986**, *43*, 2070–2087. doi: 10.1175/1520-0469(1986)043<2070:AAOTIO>2.0.CO;2
27. Mullen, S. Transient eddy forcing of blocking flows. *J. Atmos. Sci.* **1987**, *44*, 3–22. doi: 10.1175/1520-0469(1987)044<0003:TEFOBF>2.0.CO;2
28. Swanson, K. Stationary wave accumulation and the generation of low-frequency variability on zonally varying flows. *J. Atmos. Sci.* **2000**, *57*, 2262–2280. doi: 10.1175/1520-0469(2000)057<2262:SWAATG>2.0.CO;2
29. Luo, D. A barotropic envelope Rossby soliton model for block-eddy interaction. Part I: Effect of topography. *J. Atmos. Sci.* **2005**, *62*, 5–21. doi: 10.1175/1186.1
30. Barnes, E. A.; Slingo, J.; Woollings, T. A methodology for the comparison of blocking climatologies across indices, models and climate scenarios. *Climate Dynamics* **2012**, *38*, 2467–2481. doi: 10.1007/s00382-011-1243-6
31. Barnes, E. A.; Dunn-Sigouin, E.; Masato, G.; Woollings, T. Exploring recent trends in Northern Hemisphere blocking. *Geophys. Res. Lett.* **2014**, *41*, 638–644. doi: 10.1002/2013GL058745
32. Andrews, D. G. A finite-amplitude Eliassen–Palm theorem in isentropic coordinates. *J. Atmos. Sci.* **1983**, *40*, 1877–1883. doi: 10.1175/1520-0469(1983)040<1877:AFAEPT>2.0.CO;2
33. Nakamura, N.; Solomon, A. Finite-Amplitude Wave Activity and Mean Flow Adjustments in the Atmospheric General Circulation. Part I: Quasigeostrophic Theory and Analysis. *J. Atmos. Sci.* **2010**, *67*, 3967–3983. doi: 10.1175/2010JAS3503.1
34. Nakamura, N.; Zhu, D. Finite-amplitude wave activity and diffusive flux of potential vorticity in eddy-mean flow interaction. *J. Atmos. Sci.* **2010**, *67*, 2701–2716. doi: 10.1175/2010JAS3432.1
35. Lubis, S. W.; Huang, C. S. Y.; Nakamura, N.; Omrani, N.; Jucker, M. Role of Finite-Amplitude Rossby Waves and Nonconservative Processes in Downward Migration of Extratropical Flow Anomalies. *J. Atmos. Sci.* **2018**, *75*, 1385–1401. doi: 10.1175/JAS-D-17-0376.1
36. Norton, W. A. Breaking Rossby waves in a model stratosphere diagnosed by a vortex-following coordinate system and a technique for advecting material contours. *J. Atmos. Sci.*, **51**, 654–673. doi: 10.1175/1520-0469(1994)051<0654:BRWIAM>2.0.CO;2
37. Huang,C. S. Y.; Nakamura, N. Local wave activity budgets of the wintertime Northern Hemisphere: Implication for the Pacific and Atlantic storm tracks. *Geophys. Res. Lett.* **2017**, *44*, 5673–5682. doi: 10.1002/2017GL073760
38. Chen, G.; Lu, J.; Burrows, D. A.; Leung, L. R. Local finite-amplitude wave activity as an objective diagnostic of midlatitude extreme weather. *Geophys. Res. Lett.* **2015**, *42*, 10952–10960. doi: 10.1002/2015GL066959
39. Xue, D.; Lu, J.; Sun, L.; Chen, G.; Zhang, Y. Local increase of anticyclonic wave activity over northern Eurasia under amplified Arctic warming. *Geophys. Res. Lett.* **2017**, *44*, 3299–3308. doi: 10.1002/2017GL072649
40. Tibaldi, S.; Molteni, F. On the Operational Predictability of Blocking. *Tellus* **1990**, *42A*, 343–365. doi: 10.3402/tellusa.v42i3.11882
41. Scherrer, S.; Croci-Maspoli, M.; Schwierz, C.; Appenzeller, C. Two-dimensional indices of atmospheric blocking and their statistical relationship with winter climate patterns in the Euro-Atlantic region. *Int. J. Climatol.* **2006**, *26*, 233-249. doi: 10.1002/joc.1250
42. Davini, P. Atmospheric blocking and winter mid-latitude climate variability. Ph.D. thesis, Università Ca' Foscari, Venezia (Ca' Foscari University of Venice), 2013.
43. D'Andrea, F.; Tibaldi, S.; Blackburn, M. et al. Northern Hemisphere atmospheric blocking as simulated by 15 atmospheric general circulation models in the period 1979-1988. *Climate Dynamics* **1998**, *14*, 385–407. doi: 10.1007/s003820050230
44. Volodin, E. M.; Diansky, N. A.; Gusev, A. V. Simulation and Prediction of Climate Changes in the 19th to 21st Centuries with the Institute of Numerical Mathematics, Russian Academy of Sciences, Model of the Earth's Climate System. *Izvestiya. Atmospheric and Oceanic Physics* **2013**, *49*, 347–366. doi: 10.7868/S000235151304010X
45. Galin, V.Ya. Parametrization of radiative processes in the DNM atmospheric model. *Izvestiya. Atmospheric and Oceanic Physics* **1998**, *34*, 339–347.
46. Shaw, T.A. Mechanisms of Future Predicted Changes in the Zonal Mean Mid-Latitude Circulation. *Curr Clim Change Rep* **2019**, 5, 345–357. doi: 10.1007/s40641-019-00145-8
47. Francis, J.A.; Vavrus S.J. Evidence linking Arctic amplification to extreme weather in mid-latitudes. *Geophys. Res. Lett.* **2012**, *39*, L06801. doi: 10.1029/2012GL051000

48. Screen, J.A.; Simmonds I. Amplified mid-latitude planetary waves favour particular regional weather extremes. *Nat. Clim. Change* **2014**, *4*, 704–709. doi: 10.1038/nclimate2271
49. Nakamura, N.; Huang, C.S.Y. Atmospheric blocking as a traffic jam in the jet stream. *Science* **2018**, *eaat0721*. doi: 10.1126/science.aat0721
50. Nakamura, H.; Lin, G.; Yamagata T. Decadal climate variability in the North Pacific during the recent decades. *Bull. Am. Meteorol. Soc.* **1997**, 78, 2215–2225. doi: 10.1175/1520-0477(1997)078<2215:DCVITN>2.0.CO;2
51. Wiedenmann, J.; Lupo, A.; Mokhov, I.; Tikhonova, E. The Climatology of Blocking Anticyclones for the Northern and Southern Hemispheres: Block Intensity as a Diagnostic. *J. Climate* **2002**, *15*, 3459–3473. doi: 10.1175/1520-0442(2002)015<3459:TCOBAF>2.0.CO;2
52. Screen, J.A.; Deser, C.; Smith, D.M.; Zhang, X.; Blackport, R.; Kushner, P.J.; Oudar, T.; McCusker, K.e.; Sun, L. Consistency and discrepancy in the atmospheric response to Arctic sea-ice loss across climate models. *Nature Geosci* **2018**, *11*, 155–163. doi: 10.1038/s41561-018-0059-y
53. Hoskins, B. J.; Hodges, K. I. New perspectives on the Northern Hemisphere winter storm tracks. *J. Atmos. Sci.* **2002**, *59*, 1041–1061. doi: 10.1175/1520-0469(2002)059<1041:NPOTNH>2.0.CO;2
54. Held, I. M.; Ting, M.; Wang, H. Northern winter stationary waves: Theory and modeling. *J. Clim.* **2002**, *15*, 2125–2144. doi: 10.1175/1520-0442(2002)015<2125:NWSWTA>2.0.CO;2
55. Wilson, C.; Sinha, B.; Williams, R. G. The effect of ocean dynamics and orography on atmospheric storm tracks. *J. Clim.* **2009**, *22*, 3689–3702. doi: 10.1175/2009JCLI2651.1
56. Nakamura, H. Midwinter suppression of baroclinic wave activity in the Pacific. *J. Atmos. Sci.* **1992**, *49*, 1629–1642. doi: 10.1175/1520-0469(1992)049<1629:MSOBWA>2.0.CO;2
57. Deser, C.; Phillips, A.S.; Bourdette, V.; Teng, H. Uncertainty in climate change projections: the role of internal variability. *Climate Dyn.* **2012**, *38*, 527–546. doi: 10.1007/s00382-010-0977-x
58. Schiemann, R.; Athanasiadis, P.; Barriopedro, D.; Doblas-Reyes, F.; Lohmann, K.; Roberts, M.J.; Sein, D.V.; Roberts, C.D.; Terray, L.; Vidale, P.L. Northern Hemisphere blocking simulation in current climate models: evaluating progress from the Climate Model Intercomparison Project Phase 5 to 6 and sensitivity to resolution. *Weather Clim. Dynam.* **2020**, *1*, 277–292. doi: 10.5194/wcd-1-277-2020
59. Yao, Y.; Luo, D.; Dai, A.; Simmonds, I. Increased quasi stationarity and persistence of winter Ural blocking and Eurasian extreme cold events in response to Arctic warming. Part I: insights from observational analyses. *J. Climate* **2017**, *30*, 3549–3568. doi: 10.1175/JCLI-D-16-0261.1